Self-consistent determination of the band offsets in $InAs_xP_{1-x}$/InP strained-layer quantum wells and the bowing parameter of bulk $InAs_xP_{1-x}$

M. Beaudoin* and A. Bensaada
Groupe de Recherches en Physique et Technologie des Couches Minces (GCM) and Département de Génie Physique, École Polytechnique, Case Postale 6079 Succursale "Centre-Ville," Montréal, Québec, Canada H3C 3A7

R. Leonelli
Groupe de Recherches en Physique et Technologie des Couches Minces (GCM) and Département de Physique, Université de Montréal, Case Postale 6128 Succursale "Centre-Ville," Montréal, Québec, Canada H3C 3J7

P. Desjardins, R. A. Masut, and L. Isnard
Groupe de Recherches en Physique et Technologie des Couches Minces (GCM) and Département de Génie Physique, École Polytechnique, Case Postale 6079 Succursale "Centre-Ville," Montréal, Québec, Canada H3C 3A7

A. Chennouf
Groupe de Recherches en Physique et Technologie des Couches Minces (GCM) and Département de Physique, Université de Montréal, Case Postale 6128 Succursale "Centre-Ville," Montréal, Québec, Canada H3C 3J7

G. L'Espérance
Centre de Caractérisation Microscopique des Matériaux (CM)^2 and Département de Métallurgie et de Génie des Matériaux, École Polytechnique, Case Postale 6079 Succursale "Centre-Ville," Montréal Québec, Canada H3C 3A7

(Received 3 August 1995)

Low- and room-temperature optical absorption spectra are presented for a series of $InAs_xP_{1-x}$/InP strained-layer multiple quantum well structures ($0.11 \leqslant x \leqslant 0.35$) grown by low-pressure metal-organic vapor phase epitaxy using trimethylindium, tertiarybutylarsine, and phosphine as precursors. The well widths and compositions in these structures are exactly determined from the use of both high-resolution x-ray diffraction and transmission electron microscopy on the same samples. The absorption spectra are then analyzed by self-consistently fitting, for the five samples, the excitonic peak energy positions with transition energies determined from a solution to the Schrödinger equation in the envelope function formalism using the well-known Bastard/Marzin model [J. Y. Marzin *et al.*, in *Semiconductors and Semimetals*, edited by Thomas P. Pearsall, (Academic, New York, 1990), Vol. 32, p. 56]. From these self-consistent fits, both the bowing parameter of bulk unstrained $InAs_xP_{1-x}$ and the band offsets of the heterostructures are deduced self-consistently. The conduction-band offsets thus determined represent $75\% \pm 3\%$ of the total strained band-gap differences at both low (liquid He) and room temperatures. These values of the band offsets are consistent with the predictions of the quantum dipole model [J. Tersoff, Phys. Rev. B **30**, 4874 (1984)]. The values determined for the bowing parameters are found to differ slightly between 0.10 ± 0.01 eV at low temperature and 0.12 ± 0.01 eV at room temperature.

INTRODUCTION

$InAs_xP_{1-x}$/InP strained-layer multiple quantum well structures (SLMQW) are of increasing practical interest, as they are predicted to have the optimal valence-band structure for strained-layer quantum well lasers operating in the 1.3–1.55-μm wavelengths,[1–3] as well as being considered for applications in high-speed devices. In particular, optical modulators[4–8] and strained-layer quantum well lasers[9,10] have been demonstrated in this system. Of primary importance in the design of quantum well devices based on these structures are the structural control[2,11] and material parameters, such as band gap and band offset,[12–14] which represent the basis of band-gap engineering.

The band offsets are usually deduced from a theoretical fit to experimental optical transitions measured by photoluminescence, photoluminescence excitation, or optical absorption. These fits rely on the structural parameters—well thickness, alloy composition, and strain—and other material parameters—band gap, elastic coefficients, effective masses, etc.—taken from the literature. Aside from the band gap, the $InAs_xP_{1-x}$ alloy material parameters are determined from a simple linear interpolation between the widely used values of the related binaries InP and InAs. The III-V ternary alloy band gap has a parabolic dependence on the composition, the coefficient c of which is called the bowing parameter. For $InAs_xP_{1-x}$, c is not well established. For example, literature values quoted vary between 0.091 (Ref. 15) and 0.36 eV (Ref. 16) at liquid-He temperatures with similar variations reported at room temperature.[16]

In this paper, we present a structural characterization of five $InAs_xP_{1-x}$/InP SLMQW structures, grown by low-pressure metal-organic vapor phase epitaxy (LP-MOVPE). The sample structures are determined using both high-

TABLE I. Structural and optical properties of the $InAs_xP_{1-x}$/InP SLMQW samples. L_A and L_B refer to the well and barrier thickness in Å, as determined from TEM and HRXRD, δE_C is the conduction-band offset as described in Fig. 5, as a percentage of the strained structures band-gap differences, E_{XH} and E_{XL} are the heavy-hole and light-hole excitonic binding energies, respectively, and δE_C(QD) is the band offset calculated using the quantum dipole model.

			$T=8$ K				$T=300$ K				
Sample No.	Description $L_A/L_B\times$No. QW	x (%As) $\pm0.5\%$	$\delta E_C\pm3\%$ ($\%\delta E_g$)	$\delta E_C\pm5$ (meV)	E_{XH} (meV)	E_{XL} (meV)	$\delta E_C\pm3\%$ ($\%\delta E_g$)	$\delta E_C\pm5$ (meV)	E_{XH} (meV)	E_{XL} (meV)	δE_C (QD) (meV)
$InAs_xP_{1-x}$53	68/304×10	11.0	72	78	7	5	72	79	6		80
$InAs_xP_{1-x}$51	73/321×10	17.7	75	131	7	4	78	136	6	4	128
$InAs_xP_{1-x}$59	55/240×10	19.5	72	138	7	4	75	144	12		141
$InAs_xP_{1-x}$54	73/321×10	26.5	78	202	4	2	79	205	3	2	190
$InAs_xP_{1-x}$58	42/233×5	35.0	75	256	4	1	78	261	11	4	251

resolution x-ray-diffraction (HRXRD) measurements and transmission electron microscopy (TEM) observations to validate the fits to the HRXRD, with the dynamical diffraction theory. Even though low-temperature optical measurements are clearer and allow a better understanding of the underlying physics, devices are normally expected to operate near room temperature. Therefore, both low- (8 K) and room-temperature optical-absorption measurements are presented for the five samples, which are seen to exhibit well-resolved excitonic transitions at both temperatures. The optical transitions are fitted with a solution to the Schrödinger equation in the envelope function formalism, using the well-known Bastard/Marzin model.[17,18] To overcome the limitations set by the unknown bowing parameter, the five samples are fitted in a self-consistent manner.[13] Following Zhao *et al.*,[19] the temperature dependence of the strain effects have been included in the model by using the values of the lattice parameters tabulated by Sirota and collaborators.[20]

GROWTH AND STRUCTURAL CHARACTERIZATION

The SLMQW samples are grown in a horizontal cold-wall quartz reactor with a graphite susceptor equipped with a fast switching run-vent manifold with minimized dead volume. The gas switching is computer controlled and the interruption sequence has been optimized as described in previous publications.[2,11] The growth is carried out on Fe- and S-doped InP(001) substrates, using trimethylindium (TMIn) as the group-III precursor and phosphine (PH_3) and tertiary-butylarsine (TBAs) as group-V sources. The samples are grown at 600 °C and 40-Torr pressure, using Pd-purified H_2 as carrier gas with a total flow rate of 3000 SCCM (denotes cubic centimeter per minute at STP) in the reactor. These growth conditions give samples with excellent surface morphologies as no defects are observed at a magnification of 1000×, using Nomarski optical microscopy.

Each sample consists of a 7000-Å InP buffer layer followed by a 5–10 period $InAs_xP_{1-x}$/InP SLMQW structure and is capped with a 1200-Å InP layer. The thicknesses of the wells vary between 42 and 73 Å, with alloy compositions $0.11\leqslant x\leqslant0.35$. The barrier thicknesses and number of periods are chosen so that the Matthews and Blakeslee[21] critical thickness is never exceeded. The sample structures are summarized in Table I.

The sample structures are determined from both TEM and HRXRD measurements and theoretical fits. Symmetric (004) rocking curves were carried out on a Philips high-resolution five-crystal diffractometer, using the Cu $K\alpha_1$ radiation with the monochromator aligned in its Ge(220) settings.[22] These rocking curves are then analyzed using a computer simulation program developed by Fewster based on the dynamical diffraction theory.[23] Figure 1 shows a typical[24] HRXRD curve along with the fit (bottom shifted line) for sample No. 51. On such curves, the displacement of the first-order diffraction peak from the main (substrate) peak depends on the average perpendicular lattice parameter caused by the tetragonal distortion of the strained-multilayer structure. This distorted lattice parameter depends on both the $InAs_xP_{1-x}$ well composition and the relative thicknesses of the $InAs_xP_{1-x}$/InP double layer. Two free parameters are then left in the fit. In principle, one can eliminate one of these parameters by using the growth conditions if the growth rate of one of the layers is known accurately. This procedure, however, is sensitive to experimental variations in the growth rates, which may arise between different growth runs. We have chosen instead to determine the relative growth rates of

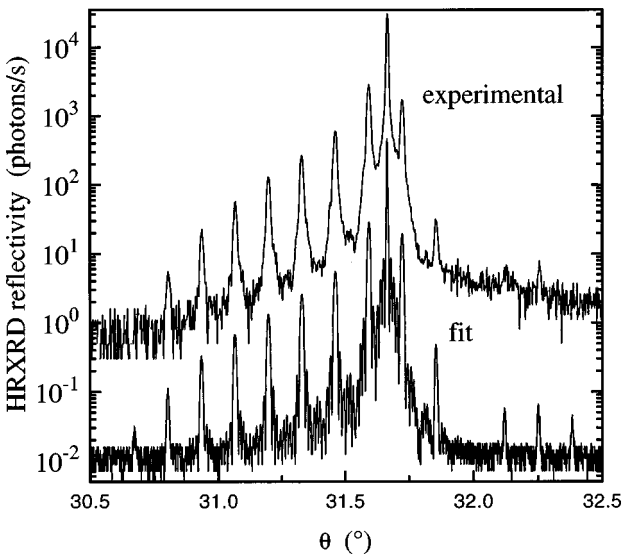

FIG. 1. HRXRD (004) reflection and fit with the dynamical diffraction theory assuming perfectly abrupt interfaces for sample No. 51. The theoretical curve has been shifted down by 100 photons/s for clarity.

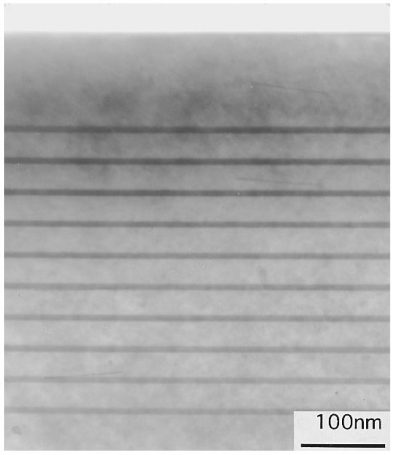

FIG. 2. Cross-sectional TEM bright-field ($g=002$) image of sample No. 51.

the $InAs_xP_{1-x}$ and InP layers in the same growth run by using TEM measurements.

Samples with ⟨110⟩ surface normals were prepared for cross-sectional TEM by conventional mechanical grinding followed by low-angle (4°) argon-ion milling at 5 keV in a Gatan precision ion polishing system. The ion energy is gradually reduced to 2.5 keV during the last stages of thinning to minimize sample damage. Figure 2 shows a TEM bright-field ($g=002$) image of sample No. 51 (see note 24 below). The double-layer thickness agrees with the one deduced from HRXRD within the TEM accuracy. TEM observations were performed on all samples and show that the structures are free of dislocations and have clearly defined and parallel quantum wells. These observations also verified that the growth rates of both the $InAs_xP_{1-x}$ and InP layers are the same for x up to 0.35 as is expected for mass transport limited LP-MOVPE growth. This allows the elimination of one of the free parameters—relative thicknesses of the $InAs_xP_{1-x}$/InP double layer—of the HRXRD fits.

Figure 1 shows the excellent fit to the curve thus obtained when perfectly abrupt interfaces between the $InAs_xP_{1-x}$ quantum wells and InP barriers are assumed. The HRXRD fits were performed on all samples and gave the structural parameters recorded in Table I. It can be observed from Fig. 1 that the experimental higher-order satellite peaks are less intense and slightly larger than those predicted by the dynamical theory. This may indicate that the interfaces are not perfectly abrupt.

OPTICAL ABSORPTION

Optical-absorption measurements were performed at 8 K in a He flow cryostat and at room temperature using a Bomem DA3 Fourier transform infrared spectrometer (FTIR). Figures 3 and 4 show the optical-absorption spectra for the five samples at low and room temperatures, respectively. At low temperature, each sample shows at least two well-resolved excitonic peaks, whereas at room temperature, at least one optical transition is always observed. The energy positions of the absorption peaks are adjusted with a solution to the Schrödinger equation in the envelope function formalism based on Kane[25] bands developed by Bastard, Marzin,

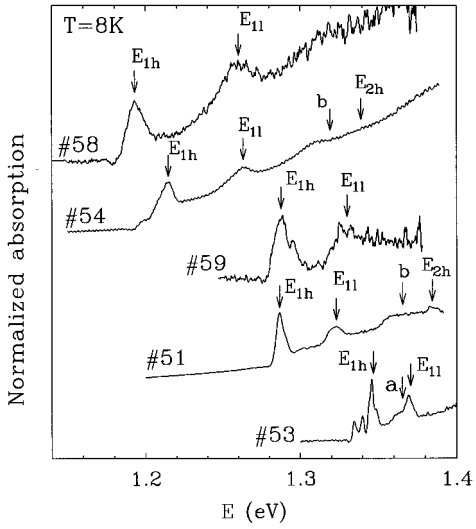

FIG. 3. Low-temperature optical-absorption data for the five sample set showing the fits (short arrows) with the envelope function model. The labels are explained in the text.

and collaborators.[17,18,26] In Marzin's version of the Bastard model, the perturbation due to the strain, along with the perturbations due to band coupling and the superlattice potential along the z direction, are included directly in the initial Hamiltonian. This leads to an 8×8 matrix secular equation which has, for each band, solutions of the Kronig-Penney form[17,18,26] when the continuity of the wave functions and probability currents are imposed at the interfaces between the wells (A material) and barriers (B material):

$$\cos q(L_A+L_B)=\cos K_A L_A \cosh K_B L_B - \frac{1}{2}\left(\bar{w}-\frac{1}{\bar{w}}\right)\sin K_A L_A \sinh K_B L_B , \qquad (1)$$

where L_A and L_B refer to the well and barrier thicknesses, respectively, while K and $\bar{w}$ are given in terms of the energy

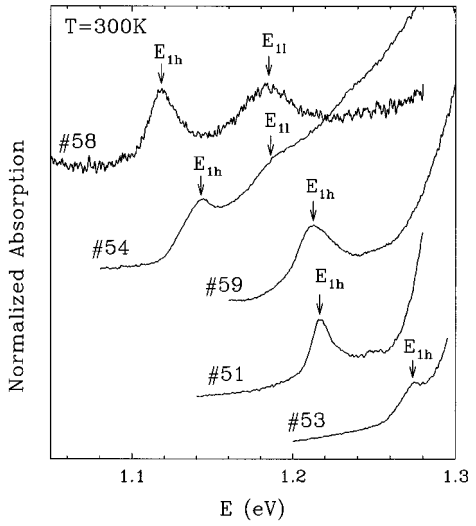

FIG. 4. Room-temperature optical-absorption data for the five sample set showing the fits (short arrows) with the envelope function model. The labels are explained in the text.

TABLE II. Low- and room-temperature physical constants for the InP and InAs binary compounds.

	InP		InAs	
Parameter	$T=8$ K	$T=300$ K	$T=8$ K	$T=300$ K
C_{11} ($\times 10^{11}$ dyn/cm^2)	10.8[a]	10.3[a]	8.33[b]	8.02[a,b]
C_{12} ($\times 10^{11}$ dyn/cm^2)	6.08[a]	5.83[a]	4.53[b]	4.41[a,b]
a (eV)	-8[a]	-8[a]	-6[b]	-6[b]
b (eV)	-1.55[a]	-1.55[a]	-1.8[b]	-1.8[b]
m_e^*/m_0	0.079[c]	0.079[c]	0.023[c]	0.023[c]
m_{hh}^*/m_0	0.65[b]	0.65[b]	0.41[b]	0.41[b]
m_{lh}^*/m_0	0.12[b]	0.12[b]	0.025[b]	0.025[b]
Δ (eV)	0.108[c]	0.108[c]	0.38[c]	0.38[c]
$E_p=2m_0P^2$ (eV)	17[c]	17[c]	21.11[c]	21.11[c]
a_0 (Å)	5.8658[d]	5.8683[d]	6.0536[d]	6.0579[d]
E_g (eV)	1.4236[c]	1.351[b]	0.418[c]	0.36[b]

[a]Reference 17.
[b]Reference 14.
[c]Reference 16.
[d]Reference 18.

E and the energy- (and material-) dependent effective mass $m_{A,B}$ by

$$E=\frac{\hbar^2K_{A,B}^2}{2m_{A,B}} \quad \text{and} \quad \bar{w}=\frac{K_Am_B}{K_Bm_A}. \tag{2}$$

The energy and effective mass in each layer depend on the strain and are coupled by the dispersion relations:[17,18,26]

$$(E-\delta E_H^A)[(E+E_g^A-\tfrac{1}{2}\delta E_S^A)(E+E_g^A+\Delta_A)-\tfrac{1}{2}(\delta E_S^A)^2]$$
$$=\hbar^2K_A^2P^2[E+E_g^A+\tfrac{2}{3}\Delta_A-\tfrac{5}{6}\delta E_S^A] \tag{3}$$

and

$$(E-V_S-\delta E_H^B)[(E-V_S+E_g^B-\tfrac{1}{2}\delta E_S^B)(E-V_S+E_g^B+\Delta_B)$$
$$-\tfrac{1}{2}(\delta E_S^B)^2]=\hbar^2K_B^2P^2[E-V_S+E_g^B+\tfrac{2}{3}\Delta_B-\tfrac{5}{6}\delta E_S^B]. \tag{4}$$

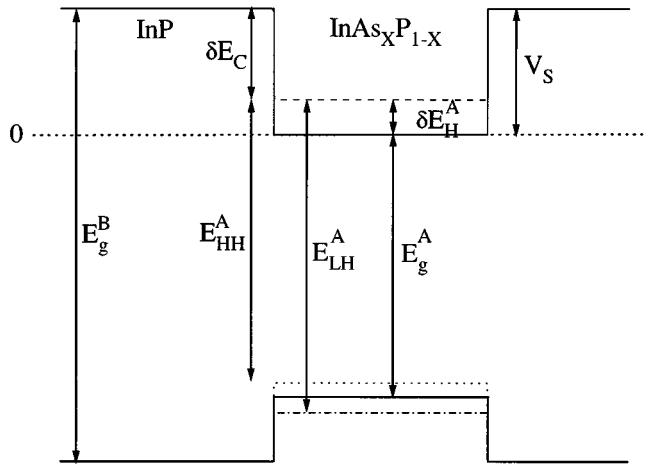

FIG. 5. Band structure of the $InAs_xP_{1-x}$/InP SLMQW structures showing the relationships between the different parameters used in the envelope function model.

In Eqs. (1)–(4), the energy origin is taken at the bottom of the *unstrained* quantum well conduction band, V_S is the band offset between the *unstrained* A and B layers, $\hbar$ is Planck's constant, $\Delta_{A,B}$ is the spin-orbit splitting, and P^2 is the material-dependent Kane matrix element, the values of which are given in Table II for the InP and InAs binary compounds. For the A and B materials, the strained heavy-hole and light-hole band gaps, $E_{\rm HH}^{A,B}$ and $E_{\rm LH}^{A,B}$, respectively, are given as corrections to the *unstrained* band gap $E_g^{A,B}$ by the usual Pikus and Bir Hamiltonian as[27]

$$\delta E_H^{A,B}=2a^{A,B}\left(\frac{C_{11}^{A,B}-C_{12}^{A,B}}{C_{11}^{A,B}}\right)\varepsilon^{A,B},$$

$$\delta E_S^{A,B}=b^{A,B}\left(\frac{C_{11}^{A,B}+2C_{12}^{A,B}}{C_{11}^{A,B}}\right)\varepsilon^{A,B},$$

$$E_{\rm HH}^{A,B}=E_g^{A,B}+\delta E_H^{A,B}-\delta E_S^{A,B},$$

$$E_{\rm LH}^{A,B}=E_g^{A,B}+\delta E_H^{A,B}+\tfrac{1}{2}[\delta E_S^{A,B}+\Delta_{A,B}]$$
$$-\tfrac{1}{2}[\Delta_{A,B}^2-2\delta E_S^{A,B}\Delta_{A,B}+9(\delta E_S^{A,B})^2]^{1/2}, \tag{5}$$

where

$$\varepsilon^{A,B}=\left(\frac{a_0^{\rm sub}-a_0^{A,B}}{a_0^{A,B}}\right) \tag{6}$$

is the biaxial strain induced by the mismatch between the substrate with a lattice parameter $a_0^{\rm sub}$ and the lattice parameter $a_0^{A,B}$ of the A or B layers. This strain varies between -0.35% ($x=0.11$) and -1.1% ($x=0.35$) for the five sample set. The hydrostatic and shear deformation potentials, $a^{A,B}$ and $b^{A,B}$ in Eq. (5), are assumed to be independent of temperature, while the elastic stiffness constants, $C_{11}^{A,B}$ and $C_{12}^{A,B}$, are temperature dependent.[19,28,29] Aside from the band gap, the materials parameters for the $InAs_xP_{1-x}$ ternary alloys are linearly interpolated between those of the InP and InAs binaries summarized in Table II. The $InAs_xP_{1-x}$ relaxed band gap is given by

$$E_g^A(x)=E_g^{\rm InP}+(E_g^{\rm InAs}-E_g^{\rm InP}-c)x+cx^2, \tag{7}$$

where the bowing parameter c is not known in general and may be temperature dependent. The relationships between the strained band-gap offset δE_C, V_S and the various parameters of Eqs. (3)–(6) are shown schematically in Fig. 5. In our case, the B layer, InP, is unstrained as it corresponds to the substrate and simplifies the band structure with $\delta E_H^B=\delta E_S^B=0$.

For a given c, the results of the structural characterization allows the calculation of Eqs. (5) and (6). With a given value of the band offset δE_C [or actually V_S in Eq. (4)], the energy is varied from the bottom to the top of the quantum wells corresponding to the conduction, light-hole, and heavy-hole bands. For each energy value, Eqs. (2)–(4) are solved and the values of $\bar{w}$, K_A, and K_B are introduced into Eq. (1), which yields a series of n roots corresponding to the n quantized levels in the conduction band and light-hole bands. Since the heavy-hole band is decoupled from the other three bands, its effective mass is energy independent and only Eqs. (1) and (2) need to be solved. The split-off band is neglected,

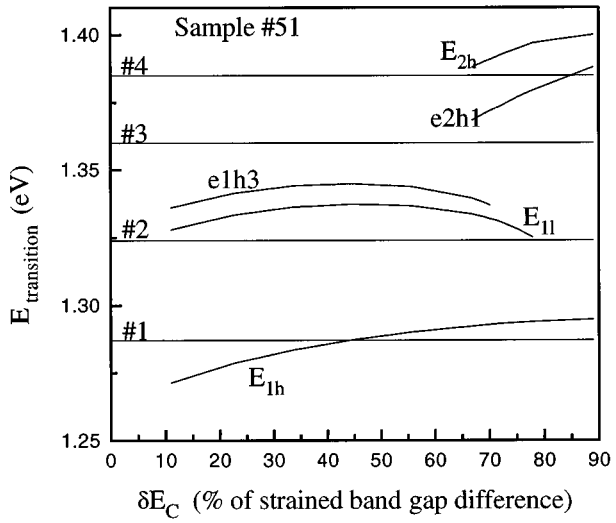

FIG. 6. Illustration of the fitting procedure used for sample No. 51 at low temperature. The horizontal lines labeled # 1–4 correspond to the experimentally observed optical transitions peaks. The energy-dependent lines correspond to various allowed and forbidden transitions, as predicted by the Marzin/Bastard model when the excitonic effects are neglected. This figure clearly shows that the best fit is obtained for $\delta E_C = 75\%$ of the strained band-gap difference.

as it would lead to transitions at much higher energies. Allowed optical transitions are those for which Δn is even, while those for which $\Delta n = 0$ will give rise to the more intense transitions.[18] Moreover, for a type-I band alignment, the transitions between the nth quantized levels in the heavy-hole and conduction bands (labeled E_{nh}) are three times more intense than those between the nth quantized levels in the light-hole and conduction bands (labeled E_{nl}).[18]

For a given c value, the fitting procedure consists in solving Eqs. (1)–(7) with the band offset δE_C as the fitting parameter, which is varied between 0% (no offset between the conduction bands) and 90% of the strained band-gap differences (at which point the light-hole band has changed from a type-I to a type-II alignment). Figure 6 illustrates the procedure for the low-temperature data of sample No. 51, where the experimentally determined optical transitions (Nos. 1–4 correspond to the four peaks visible on Fig. 3) are compared to various allowed transitions—and one forbidden transition—predicted by the model with the excitonic binding energies neglected. Note that no light-hole related transitions are predicted for δE_C above 78% and no experimental $e1h3$ predicted transitions (between the $n=3$ heavy-hole and the $n=1$ electronic levels) for δE_C above 70% are observed. This effectively sets lower and higher limits on the possible values that δE_C can take. This fitting procedure allows the identification of the optical transitions and a measure of the excitonic binding energies defined here as the energy difference between the predicted and measured optical transitions. Due to the differences in effective masses, heavy-hole excitons, E_{XH}, in *bulk* $\mathrm{InAs}_x\mathrm{P}_{1-x}$ should have a binding energy about 1.5 times larger than the light-hole excitons E_{XL}, according to the simple hydrogenic model. In practice, one can expect binding energies between the bulk values (3–6 meV) and about 10 meV for the heavy-hole excitons. With this criteria, and retaining the first two transitions as the most significant, one determines a *window* for δE_C. In the case of the low-temperature data of sample No. 51 with $c=0.10$ eV, $\delta E_C = 75\% \pm 3\%$ of the strained band-gap difference yields acceptable values of E_{XH} and E_{XL}. This procedure is used on all samples at both low and room temperatures. The values of δE_C, E_{XH}, and E_{XL} are reported in Table I. Assuming that the quadratic relationship of the band gap with the alloy composition x [Eq. (7)] holds for all compositions studied, it is imperative that all samples be fitted with the same c at a given temperature. With this restriction, c was kept as a free parameter for the five sample *set*. The energy transitions predicted by the model are superimposed on the spectra of Figs. 3 and 4 by short arrows. Acceptable self-consistent fits were possible at low temperature for $0.09 \leqslant c \leqslant 0.11$ eV and at room temperature for $0.11 \leqslant c \leqslant 0.13$ eV, but the extreme values had to be fitted with slightly different band offsets. The quoted uncertainties in δE_C are given for $c=0.10$ and 0.12 at low and room temperatures, respectively (Table I). In addition to the allowed transitions, the low-temperature spectra show additional peaks, which are labeled (a) and (b) in Fig. 3. The spectrum of sample No. 53 is particularly rich with other additional peaks (unlabeled) below the main $E_{1\mathrm{h}}$ transition peak and an elongated shoulder preceding the E_{11} peak and labeled (a).

DISCUSSION

Preliminary results on the low-temperature spectra have already been presented.[13] At the time, the spectra were fitted with a simpler Bastard model, developed for unstrained systems, in which the effects of strain were introduced by a simple modification of the band gaps with the Hamiltonian of Pikus and Bir[27] [Eqs. (5) and (6)]. This model allowed the correct assignment of the main transition peaks and gave acceptable values for δE_C. However, for higher As content in the $\mathrm{InAs}_x\mathrm{P}_{1-x}$ alloys, it was found that the excitonic binding energies were unacceptable as the light-hole excitons had a higher energy than the heavy-hole excitons.[13] Since the correct band alignment occurs when the light-hole band approaches a type-I to type-II transition, one should expect these excitons to be weakly localized and thus give rise to weak binding energies. The present model, with the effects of strain accounted for in the initial Hamiltonian improves this aspect as is evident from Table I. Moreover, the relative intensity of the light-hole and heavy-hole transitions eliminate the possibility of a type-II alignment for the light-hole bands, since the transition matrix elements would be very weak if the electrons and light holes were actually spatially separated in adjacent layer materials.[18]

In Ref. 13, we have suggested possibilities for some of the observed additional peaks in the low-temperature spectra. These peaks are labeled (a) and (b) in Fig. 3 and were attributed to forbidden transitions: (a) between the $n=2$ heavy-hole quantized level and the $n=1$ electronic level (labeled $e1h2$) and (b) between the $n=1$ heavy-hole level and the $n=2$ electronic level ($e2h1$). We had argued then that such transitions might be possible, since the strain effects may relax the selection rules. Moreover, the model used then predicted transitions very close to those observed experimentally. The present model does not predict these transitions at exactly the same energies and casts some insight on the pre-

vious assignment. The transition labeled (a) is only observed in sample No. 53, which also shows two weaker transitions below the E_{1h} peak. These peaks are not clearly understood at present, but could be attributed to interface states.[11] The peak labeled (a) can then be attributed to either the same effect or, as in Ref. 13, to an $e1h2$ forbidden transition. According to Bastard,[18] such a transition would only be possible for highly asymmetric quantum wells and has probably never been experimentally observed in symmetric quantum wells. Thus, a definite assignment of this peak is still highly speculative at this point.

The low-temperature spectra of samples Nos. 51 and 54 show the presence of higher-level transitions E_{2h} and possibly one extra transition labeled (b) in Fig. 3 attributed to an $e2h1$ forbidden transition. Figure 3 shows that sample No. 51 is very well fitted with this assignment. Here again, however, to our knowledge, such transitions have never been observed in the past and should not be observed for symmetric quantum wells. In addition, such an assignment implies the washing out of the E_{2h} transition in sample No. 54. A more likely scenario for No. 54 is that the third experimental peak is in fact due to the E_{2h} transition, but that the model fails to reproduce it. Many reasons could then be invoked for such a failure. For one, the second quantized levels penetrate deeper into the barrier regions and, therefore, feel more effects from the interfaces. This is corroborated by the fact that the Kronig-Penney model, known to fail for a large wave-function penetration into the barriers, predicts an E_{2h} transition 13 meV above the one predicted by the Bastard/Marzin model.

The analysis of the room-temperature spectra is both more straightforward, as no additional peaks are observed beyond the allowed transitions, and less precise as less peaks are observed. The five sample set was also self-consistently fitted with the model using $0.11 \leqslant c \leqslant 0.13$ eV by varying the δE_C. The best fit, with $c = 0.12$ eV, gave $\delta E_C = 75\% \pm 3\%$ of the *strained* band-gap differences between the well and barrier materials. The fitted energy transitions are shown as short arrows above the experimental transition peaks in Fig. 4. The deduced excitonic binding energies are summarized in Table I alongside the low-temperature data. The fits of the main transitions for the room-temperature data do not give excitonic binding energies as consistent as those at low temperature. This is probably due to the increased width of the optical transitions, which originates partly from thermal broadening, but possibly also from absorption by interface states. If such states are present, as we are suggesting for No. 53's small peaks below the main transition at low T, then at room temperature, these peaks would be convoluted into the main transition peak giving rise to a bias in the measured energy position. Since not all samples may exhibit these states, the self-consistent fitting procedure will also suffer from the bias and the spectra will be more difficult to fit. This difficulty, then, reflects itself in the seemingly random variations in the deduced excitonic binding energies. However, the fitted absolute values of δE_C remain at almost exactly the same value as at low temperature, while the overall type-I band alignment is preserved and the light-hole band remains very close to a type-II alignment.

Figure 7 shows the linear relationship of δE_C (absolute value in meV) with the As concentration of the $InAs_xP_{1-x}$ alloy. The low- (■) and room- (●) temperature values are almost superimposed on each other and should be considered identical within the uncertainties, due to the fitting procedure and experimental errors. To date, the best theoretical treatment of the band offsets in semiconductor heterojunctions is the quantum dipole model developed by Tersoff.[30] The central idea of this model is that there exists a band offset dependent dipole at the interface between two semiconductors, due to quantum-mechanical tunneling. The two semiconductors will tend to align in order to cancel this dipole. Tersoff thus introduces an effective midgap energy E_B which corresponds to the energy at which the wave functions of gap states change from a primarily valence like to a primarily conductionlike character. For a given material, E_B is calculated using a Green's function approach, which sums all the gap state wave functions taking into account their valence-like and conductionlike character. This approach yields E_B values of 0.50 eV and 0.76 eV for InAs and InP, respectively, where E_B is measured from the valence-band maximum. To correctly extend this model to $InAs_xP_{1-x}$ alloys, one should, in principle, calculate the value of E_B using the Green's function approach. As a first approximation, however, it is sufficient to determine E_B from a linear interpolation between the values of the InAs and InP binaries. The straight line fit in Fig. 7 shows the perfect agreement between the quantum dipole model and the δE_C determined from the fit of the Marzin/Bastard model to the optical-absorption spectra. The δE_C values predicted from the quantum dipole are reported in Table I for each sample. The agreement is such, that we find it important to note that the quantum dipole calculations were done *after* the optical spectra had been fitted with the Marzin/Bastard model and did not, therefore, influence our interpretation of the optical data. These results indicate that the quantum dipole model, which works well for other semiconductor heterojunctions,[30] is also valid for the $InAs_xP_{1-x}$/InP system.

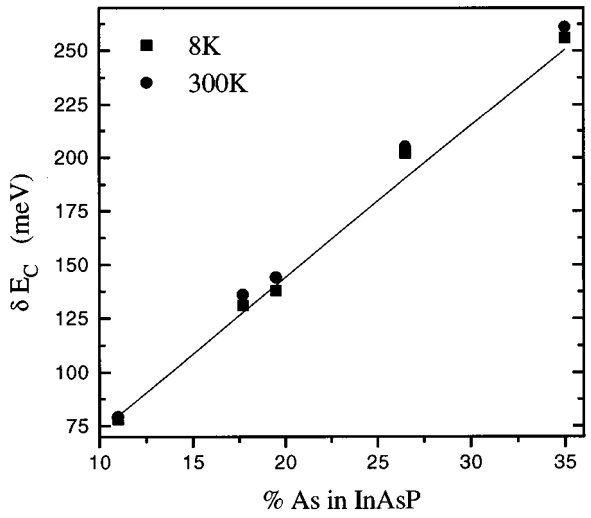

FIG. 7. Dependence of δE_C (in meV) on the As content of the $InAs_xP_{1-x}$ alloy quantum wells. Both the low- (■) and room- (●) temperature data are superimposed. The full line is generated using the quantum dipole model, as described in the text.

CONCLUSION

High structural quality SLMQW structures, as assessed by TEM and HRXRD, were grown by LP-MOVPE. In addition

to providing direct evidence of well-defined quantum wells and barriers, with abrupt interfaces, the TEM results also show that the growth rates of the $InAs_xP_{1-x}$ ternary alloy is the same as that of the InP binary compound, as is expected for mass transport limited growth. These TEM results then allow the elimination of the free parameters in the fits of the HRXRD patterns with the dynamical diffraction theory. The TEM and HRXRD analyses taken together, therefore, allow a very precise determination of both the quantum well and barrier thicknesses and the $InAs_xP_{1-x}$ alloy compositions. This information is extremely important in the further analysis of the optical data.

Low- (8 K) and room-temperature optical-absorption spectra were presented for a five sample set. A self-consistent application of the Bastard/Marzin model to the five sample set allowed both a determination of the band alignment and the bowing parameter of bulk $InAs_xP_{1-x}$. Both the low- and room-temperature spectra can be adjusted with the same *relative*, 75%±3% of strained band-gap difference, and *absolute* (in meV) band offsets with a linear relationship found between the band offsets and the As content of the $InAs_xP_{1-x}$ alloy quantum wells. The best self-consistent fits are obtained with bowing parameters $c=0.10\pm0.01$ eV at 8 K and 0.12 ± 0.01 eV at 300 K. At both temperatures, the heavy-hole band offsets are clearly type I. The light-hole offsets are also type I, but the best fit to the absorption data is obtained when the band alignment approaches a type-I to type-II transition. Finally, it is found that the quantum dipole theory of band offsets is in perfect agreement with the experimentally determined band offsets, thus indicating the validity of this model for $InAs_xP_{1-x}$/InP heterojunctions.

ACKNOWLEDGMENTS

The authors thank the Conseil de Recherches en Sciences Naturelles et en Génie du Canada (CRSNG) and the Fonds pour la Formation des Chercheurs et l'Aide à la Recherche (FCAR), Québec for financial assistance. M.B. wishes to express special thanks to the Fondation du Prêt d'Honneur (Société St-Jean Baptiste de Montréal) for support. Technical support was provided by René Lacoursière, René Veillette, and Joël Bouchard.

*Present address: Physics Department, University of British Columbia, Vancouver, BC, Canada V6T 1Z1. Electronic address: beaudoin@physics.ubc.ca

[1] E. Yablonovitch and E. O. Kane, IEEE J. Lightwave Technol. **LT-6**, 1292 (1989).

[2] C. A. Tran, J. T. Graham, R. A. Masut, and J. L. Brebner, in *Growth, Processing, and Characterization of Semiconductor Heterostructures*, edited by G. Gumbs, S. Luryi, B. Weiss, and G. W. Wicks, MRS Symposia Proceedings No. 326 (Materials Research Society, Pittsburgh, 1994), p. 115.

[3] D. R. Storch, R. P. Schneider, Jr., and B. W. Wessels, J. Appl. Phys. **72**, 3041 (1992).

[4] G. C. Osbourn, J. Vac. Sci. Technol. A **3**, 826 (1985).

[5] L. F. Palmateer, P. J. Tasker, T. Itoh, A. S. Brown, G. W. Wicks, and L. F. Eastman, Electron. Lett. **23**, 53 (1987).

[6] R. Yip, M. Beaudoin, A. Aït-Ouali, R. A. Masut, J. F. Currie, and J. L. Brebner (unpublished).

[7] T. K. Woodward, T.-H. Chiu, and Theodore Sizer II, Appl. Phys. Lett. **60**, 2848 (1992).

[8] H. Q. Hou, A. N. Cheng, H. H. Wieder, W. S. C. Chang, and C. W. Tu, Appl. Phys. Lett. **63**, 1833 (1993).

[9] H. Oohashi, T. Hirono, S. Seki, H. Sugiura, J. Nakano, M. Yamamoto, Y. Tohmori, and K. Yokoyama, J. Appl. Phys. **77**, 4119 (1995).

[10] Hideo Sugiura, Manabu Mitsuhara, Hironi Oohashi, Takuo Hirono, and Kiichi Nakashima, J. Cryst. Growth **147**, 1 (1995).

[11] C. A. Tran, J. T. Graham, J. L. Brebner, and R. A. Masut, J. Electron. Mater. **23**, 1291 (1994).

[12] S. J. Hwang, W. Shan, J. J. Song, H. Q. Hou, and C. W. Tu, J. Appl. Phys. **72**, 1645 (1992).

[13] M. Beaudoin, R. A. Masut, L. Isnard, P. Desjardins, A. Bensaada, G. L'Espérance, and R. Leonelli, in *Microcrystalline and Nanocrystalline Semiconductors*, edited by L. Brus, M. Hirose, R. W. Collins, F. Koch, and C. C. Tsal, MRS Symposia Proceedings No. 358 (Materials Research Society, Pittsburgh, 1995), p. 1005.

[14] A. Bensaada, J. T. Graham, J. L. Brebner, A. Chennouf, R. W. Cochrane, R. Leonelli, and R. A. Masut, Appl. Phys. Lett. **64**, 273 (1994).

[15] S. Adachi, J. Appl. Phys. **53**, 8775 (1982).

[16] *Physics of Group IV Elements and III-V Compounds*, edited by O. Madelung, Landolt-Börnstein, New Series, Group III, Vol. 17, Pt. a (Springer, Berlin, 1982).

[17] J. Y. Marzin, J. M. Gérard, P. Voisin, and J. A. Brum, *Strained-Layer Superlattices: Physics*, Semiconductors and Semimetals Vol. 32 (Academic, San Diego, 1990), p. 56.

[18] G. Bastard, *Wave Mechanics Applied to Semiconductor Heterostructures* (Éditions de Physique, Les Ulis, 1988).

[19] Y. G. Zhao, R. A. Masut, J. L. Brebner, C. A. Tran, and J. T. Graham, J. Appl. Phys. **76**, 5921 (1994).

[20] A. N. Sirota, A. M. Antyukhov, and A. A. Sidorov, Dok. Akad. Nauk SSSR **277**, 1379 (1984) [Sov. Phys. Dokl. **29**, 662 (1985)].

[21] J. W. Matthews and A. E. Blakeslee, J. Cryst. Growth **27**, 118 (1974).

[22] A. Bensaada, A. Chennouf, R. W. Cochrane, J. T. Graham, R. Leonelli, and R. A. Masut, J. Appl. Phys. **75**, 3024 (1994).

[23] P. F. Fewster, Philips J. Res. **45**, 620 (1984).

[24] Note that in Ref. 13, both the TEM observations and the HRXRD pattern and fit for No. 53 were presented and gave similar results.

[25] E. O. Kane, J. Phys. Chem. Solids **1**, 249 (1957).

[26] G. Ji, D. Huang, U. K. Reddy, T. S. Henderson, R. Houdré, and H. Morkoç, J. Appl. Phys. **62**, 3366 (1987).

[27] G. E. Pikus and G. L. Bir, Fiz. Tverd. Tela (Leningrad) **1**, 154 (1959) [Sov. Phys. Solid State **1**, 136 (1959)]; **1**, 1642 (1959) [**1**, 1502 (1960)].

[28] N. S. Orlova, Cryst. Res. Technol. **24**, K39 (1989).

[29] A. S. Jordan, J. Cryst. Growth **71**, 559 (1985).

[30] J. Tersoff, Phys. Rev. B **30**, 4874 (1984).